Article

Frictional Properties and Seismogenic Potential of Caprock Shales

Bahman Bohloli [1],* , **Magnus Soldal [1,2]**, **Halvard Smith [1]**, **Elin Skurtveit [1,2]** , **Jung Chan Choi [1]** **and Guillaume Sauvin [1]**

[1] Norwegian Geotechnical Institute, Sognsveien 72, 0806 Oslo, Norway; magnus.soldal@ngi.no (M.S.); halvard.smith@ngi.no (H.S.); Elin.Skurtveit@ngi.no (E.S.); jungchan.Choi@ngi.no (J.C.C.); guillaume.sauvin@ngi.no (G.S.)

[2] Department of Geosciences, University of Oslo, 0315 Oslo, Norway

* Correspondence: bahman.bohloli@ngi.no

check for
updates

Abstract: Fractures and faults are critical elements affecting the geomechanical integrity of CO_2 storage sites. In particular, the slip of fractures and faults may affect reservoir integrity and increase potential for breach, may be monitored via the resulting seismicity. This paper presents an experimental study on shale samples from Draupne and Rurikfjellet formations from the North Sea and Svalbard, Norway, using a laboratory test procedure simulating the slip of fractures and faults under realistic stress conditions for North Sea CO_2 storage sites. The motivation of the study is to investigate whether the slip along the fractures within these shales may cause detectable seismic events, based on a slip stability criterion. Using a direct shear apparatus, frictional properties of the fractures were measured during shearing, as a function of the shear velocity and applied stress normal to the fracture. We calculated the friction coefficient of the fractures during the different stages of the shear tests and analysed its dependency on shear velocity. Information on velocity-dependent friction coefficient and its evolution with increasing slip were then used to assess whether slip was stable (velocity-strengthening) or unstable (velocity-weakening). Results showed that friction coefficient for both Draupne and Rurikfjellet shales increased when the shear velocity was increased from 10 to 50 µm/s, indicating a velocity-strengthening behaviour. Such a behaviour implies that slip on fractures and faults within these formations may be less prone to producing detectable seismicity during a slip event. These results will have implications for the type of techniques to be used for monitoring reservoir and caprock integrity, for instance, for CO_2 storage sites.

Keywords: direct shear; velocity-stepping; friction; shale; CO_2 storage; seismicity

1. Introduction

Carbon capture and storage in the subsurface is considered by the Intergovernmental Panel on Climate Change (IPCC) as one of the major mitigation methods to climate change [1]. Storage reservoirs should ideally have porosity and permeability sufficient to accommodate large volumes of CO_2 injected at relatively high rates. In addition, the long-term safe disposal underground should be ensured by the confinement provided by overlying tight caprocks. For site selection and location of CO_2 injection wells, zones of high risk such as proximity to faults and major fractures should be avoided. However, large-scale CO_2 storage will require the utilization of reservoirs that are faulted (e.g., the Smeaheia fault block offshore Norway). During injection of CO_2, the pore pressure will increase. To maintain seal integrity and ensure that injected CO_2 remains within the defined storage reservoir, the operation of a storage site must be conducted in a manner that reservoir pressure does not exceed the fracture pressure, to avoid failure of the reservoir or seal units. It is usually difficult to

determine the actual fracture pressure of geological formations and therefore injection pressure may in some instances exceed the fracture pressure and cause failure during operation of a site. Failure will most likely occur along the pre-existing weakness planes, such as the pre-existing fractures or slip surfaces that are favourably orientated with respect to the local stress field and frictional properties. Frictional stability of a fracture is dependent on the host rock material, the mineral fill, or gouge present in fracture plane, and the normal and shear stresses acting on the fracture. At low normal stresses, the roughness and contact ratio of fracture surface will also contribute to the frictional strength.

Reactivation of fractures and faults in caprocks due to changes in reservoir pressure conditions and the risk of induced seismic events has been addressed in several studies e.g., [2–6]. The authors reported several cases of water injection or hydrocarbon production where faults have been reactivated both above and below the reservoir. The basic physical principle describing fault reactivation is the effective stress concept [7], conceptualized in Figure 1. To avoid undesired failure and leakage of the injected fluid, monitoring of CO_2 injection sites is essential. One of the commonly used methods is the microseismic monitoring which is the passive recording of low-magnitude earthquakes occurring in the subsurface and can be an effective method for detecting shear failure or fault reactivation. Nucleation of seismic or aseismic slip of fractures depends on several factors, among them are rock composition and frictional strength [8–16].
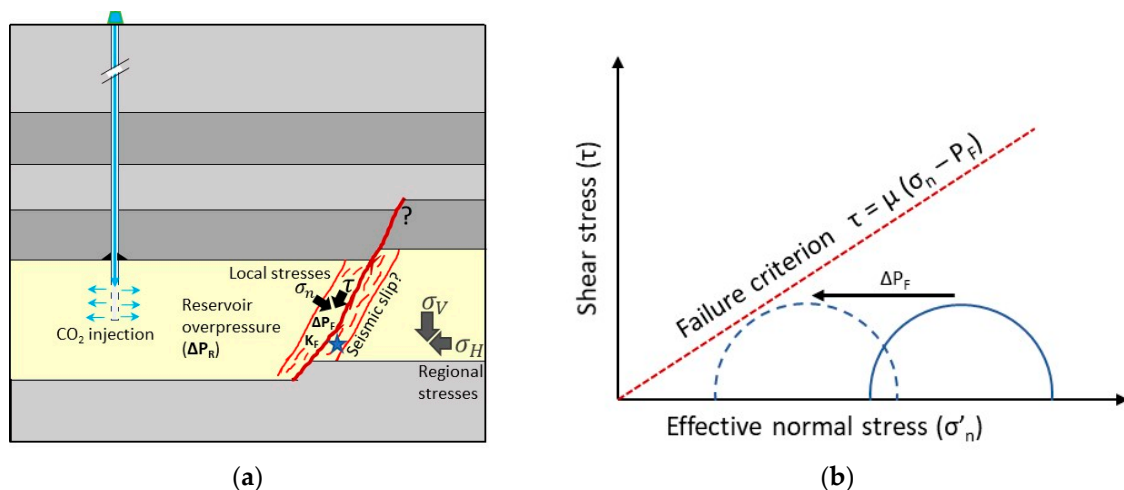

Figure 1. (**a**) Schematic presentation of CO_2 injection in a reservoir causing overpressure, ΔP_R, pore pressure inside a fault zone, ΔP_F, fault permeability, K_F, and the local normal (σ_n) and shear stresses (τ) in a fault zone. (**b**) A critical fluid pressure within a fault, ΔP_F-which may be different from the ΔP_R and can push a stable case (full circle) towards failure (dashed circle).

The potential for seismic or aseismic slip of fractures can be examined using laboratory direct shear experiments designed to determine velocity-dependence friction coefficient as described by the rate-and-state friction (RSF) law of Dieterich [17] and Ruina [18]. The Dieterich-Ruina law is an empirical method that is used to describe earthquake dynamic processes based on the static and mobilised friction of a fault at different slip velocities. This method assumes a stable slip will be aseismic while an unstable, stick-slip will be associated with seismic events. Several researchers have conducted direct shear tests to determine if dynamic friction is positively or negatively correlated with shear velocity (i.e., velocity-strengthening or velocity-weakening, respectively) [19–23]. For instance, Kohli and Zoback [20] tested several shales with different percentage of clay and organic matter contents. Shales with clay and organic contents exceeding 30 wt.% displayed velocity-strengthening behaviour, whereas shales with less clay and organic matter showed velocity-weakening and thus potential for seismic slip.

Other studies have shown that small slip events related to hydraulic fracturing within shale and tight gas reservoirs have generated seismic events recorded by microseismic monitoring. However,

the shear slip and deformation estimated from microseismic data was not enough to explain the total rock deformation as calculated from the mass balance of production history [20,24–26]. Thus, other slow slip, non-seismic deformation mechanisms may be present in shale during injection and fracture reactivation. Understanding these mechanisms requires further investigation of the fundamental mechanical behaviour of fractures during slip in shales.

Draupne shale in the North Sea and Rurikfjellet formation on Svalbard are caprocks for candidates for CO_2 storage sites and therefore, understanding failure and slip mechanisms within these formations is critical for North Sea CCS projects. Hence, there are not enough data on frictional properties of these shales to assess their frictional parameters and mechanical behaviour during a slip. This study focuses on the potential of seismicity for Draupne and Rurikfjellet shales using laboratory shear tests. Direct shear tests with varying shear velocities (velocity-step tests) were performed to measure the frictional properties of the shale samples. Laboratory data reveal whether slip along fractures in the Draupne and Rurikfjellet formations may be velocity-strengthening or -weakening, indicating whether we may expect seismic events or aseismic slip of faults within the sealing cap rock.

2. Rate and State Friction Law

One of the main indicators of the seismic potential of faulted rocks during shear failure is the evolution of frictional resistance with shear velocity, or velocity-dependent frictional behaviour [17,18]. The relationship between the friction coefficient (μ) and shear velocity (V) may be analysed in the framework of rate-and-state (RSF) friction equations [17,27]:

$$\mu = \mu_0 + a \, \ln\left(\frac{V}{V_0}\right) + b \, \ln\left(\frac{V_0 \theta}{d_c}\right) \tag{1}$$

where μ_0 is the friction coefficient (the ratio of shear stress to normal stress) determined at a reference shear velocity V_0, d_c is the critical slip distance causing renewal of the contact population (contact lifetime), and the non-dimensional parameters a and b represent the direct change in friction (a) and subsequent evolution of friction (b) following a change in shear velocity. The state variable, θ, represents the mean lifetime of a micro-contact and evolves with time as the velocity is changed according to Equation (2) [22]:

$$\frac{d\theta}{dt} = 1 - \left(\frac{V\theta}{d_c}\right) \tag{2}$$

At steady state sliding, the state variable does not change and the rate-and-state friction equation reduces to [22,28]:

$$\mu = \mu_0 + (a - b) \ln\left(\frac{V}{V_0}\right) \tag{3}$$

By rearranging Equation (3), the friction rate parameter ($a - b$) can be expressed as:

$$(a - b) = \frac{\mu - \mu_0}{\ln\left(\frac{V}{V_0}\right)} \tag{4}$$

The interpretation of parameters a and b during direct shear velocity stepping is shown schematically in Figure 2a. Increasing the shear velocity leads to an increase in friction by a. This change is called the direct (velocity) effect. Following the velocity increase, the friction coefficient decreases by b. This second change is called the evolutionary effect. If the friction coefficient at a higher shear velocity is lower than for the low shear velocity (i.e., a negative value of $a - b$), then material is velocity-weakening [29] (Figure 2a). The opposite, a positive value of $a - b$, is referred to as velocity-strengthening [18,29,30]. In case of velocity-weakening, accelerating slip may occur and generate seismicity, whereas velocity-strengthening indicates that fault rocks become stronger with increasing shear velocity and thus prevent accelerating, seismogenic slip [11,12].
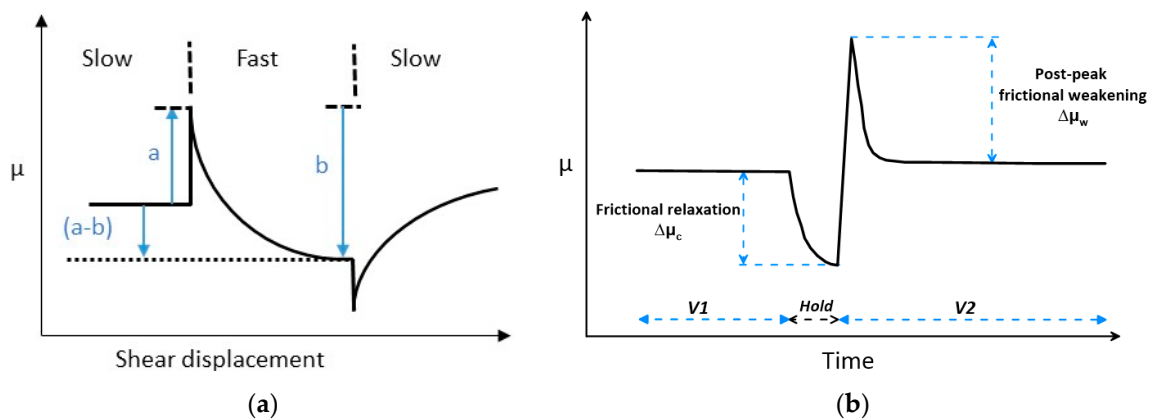
Figure 2. (**a**) A simplified rate-and-state friction model (modified after [22]). Negative values of $(a - b)$, as illustrated here, indicate velocity-weakening of the material, and implies generation of seismicity in case of a slip. Positive $(a - b)$ values indicate velocity-strengthening behaviour and imply aseismic movement during a slip. (**b**) Schematic presentation of frictional relaxation, and post-peak frictional weakening (modified after [12]).

Experimental measurements of static friction following an interruption in steady frictional sliding (simulating interseismic periods) can be obtained through a slide-hold-slide (SHS) test (for more information see [12]). A SHS test procedure includes three steps: (i) A sample is sheared until a stable slide is achieved (slide); (ii) shearing is halted for a certain period of time (hold); and (iii) another shear cycle is applied (slide). Several terms, such as frictional relaxation, frictional healing and frictional weakening are used to describe the response of material to a slide-hold-slide test. The frictional relaxation ($\Delta\mu_c$) is calculated as the difference between the steady state friction prior to hold and the minimum friction during a hold period. If steady state friction before and after the hold period is equal, the frictional healing is the difference between peak friction and pre- or post-hold friction. The difference between peak friction and post-hold steady-state friction is called post-peak frictional weakening (Figure 2b).

3. Material and Methods

3.1. Test Samples

The material used in this study consists of core samples from two shales from Draupne and Rurikfjellet formations. The Draupne Formation is an organic rich shale deposited under anoxic conditions during the Late Jurassic transgression [31], and a common source rock and seal formation in the North Sea. In the Horda Platform area, Draupne is the primary seal formation for potential carbon dioxide storage in the Sognefjord Formation within the Smeaheia fault block [32], offshore Norway. Its total clay content is about 50% and kaolinite is the major clay mineral [33–35]. The amount of carbonates varies, and the faulted core section shows relatively high calcite content (up to 24%) within certain areas of the retrieved core section [33,35] (Table 1). Large accumulations of carbonate concretions were also identified within the intact matrix (Figure 3A,B). Scanning electron microscope (SEM) images showed prominent feldspars, micas, lenses of organic material and carbonaceous microfossils, indicating a relatively immature shale (Figure 3C,D).

Table 1. Mineral composition of Draupne and Rurikfjellet shales in percentage. The sum of percentage of minerals for each sample in this table is greater than 100% which may be due to a poor detection and overlap between some of the clay minerals characterized by XRD.

Sample	Smectite	Kaolinite	Chlorite	Mica/Illite	Pyrite	Quartz	Feldspar	Calcite	Dolomite	TOC [a]
Draupne [b] ID: DST15 & DST17	9.13	31.50	0.35	9.78	7.70	22.40	17.80	0.70	1.20	~7 [c]
Rurikfjelle [d] ID: LYB22	-	12.56	9.70	21.57	0.81	40.19	6.92	8.24 [e]	-	~1.5

[a] TOC = total organic carbon, [b] after [34,35], [c] after [33], [d] after [36], [e] Siderite.
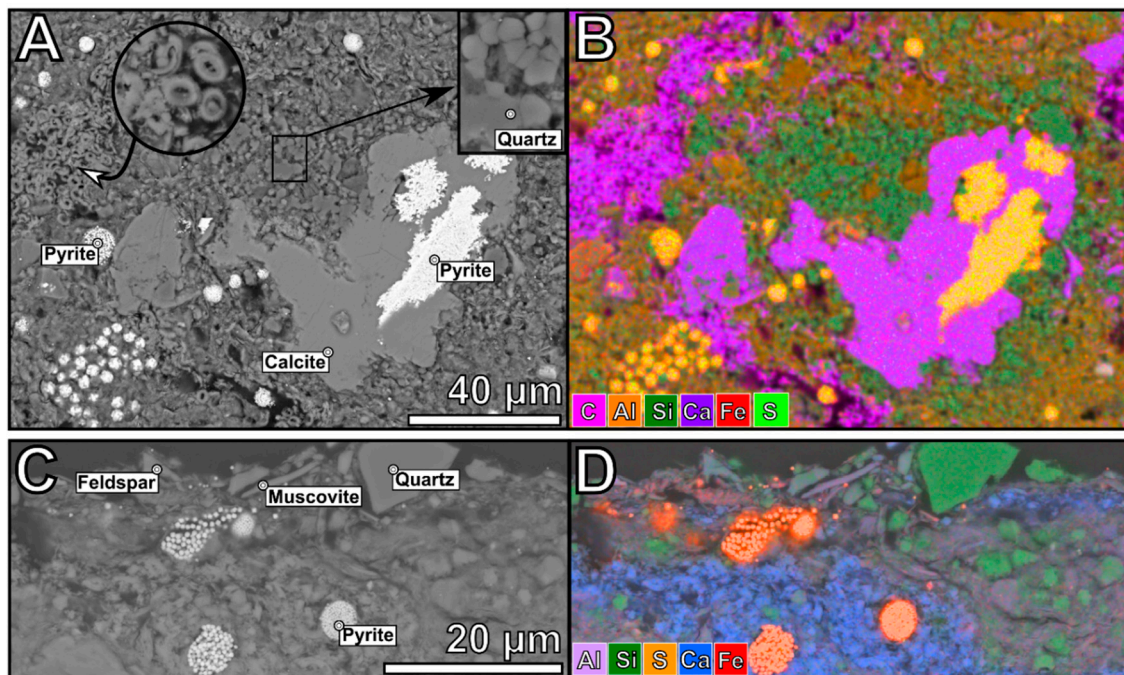
Figure 3. Scanning electron microscope (SEM) image of Draupne Shale (modified after [35]). (**A**,**B**) show the distribution of microfossils, pyrite, carbonates and quartz. Note the authigenic growth of quartz. (**C**,**D**) show the presence of detrital quartz, feldspars and micas. Note the smearing of framboidal pyrite along the shear surface. Color-coding in (**B**,**D**) indicate the position of key-elements shown in (**A**,**C**) in a grey scale, respectively. Index: C = carbon, Al = aluminium, Si = silicon, Ca = calcium, Fe = iron, S = sulphur.

The Draupne core samples were retrieved from a depth of 2575 m in the Ling Depression, the North Sea (exploration well 16/8-3S) and stored in oil prior to sample preparation and testing. From the original core diameter of about 113 mm, two specimens were prepared for testing in the direct shear box apparatus (DST15 and DST17). Specimen DST15 was cut into a rectangular shape of 65 × 75 mm and a thickness of 60 mm from a core section containing a pre-existing fracture. The fracture surface contained lineations that are evidence of slip during geological time (Figure 4C,D). DST17 specimen was slightly smaller (67 × 69 mm and thickness of 60 mm) and contained a bedding-parallel fracture. No sign of previous slip was observed for this fracture. The Draupne specimens had a natural water content of around 6–7% prior to testing.
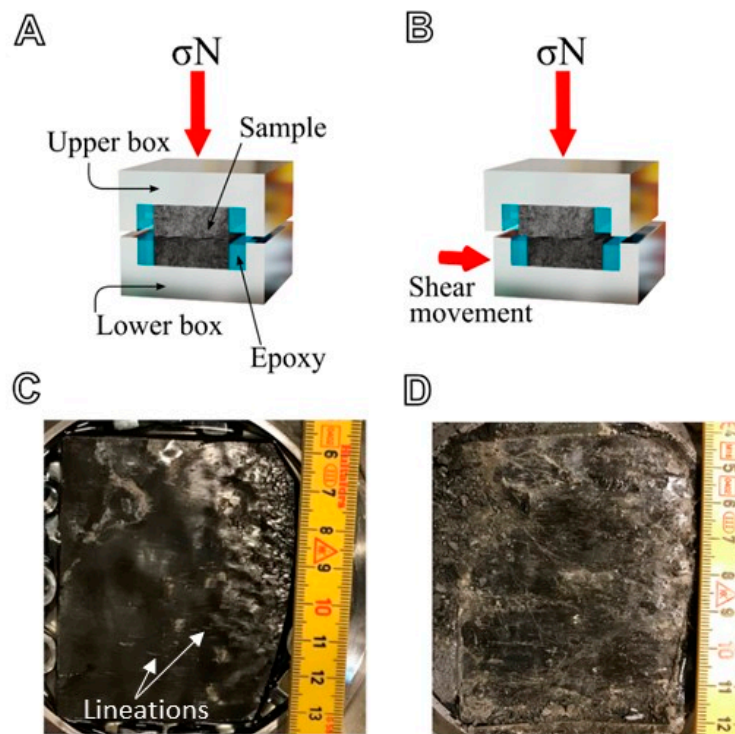
Figure 4. Schematic presentation of a direct shear test (**A**,**B**) and bottom part of a Draupne specimen-DST15 before (**C**) and after (**D**) direct shear test. Fracture surface before testing (**C**) contains lineations that are evidence of slip during geological time.

Rurikfjellet is a Lower Cretaceous shaley part of the overburden for Longyearbyen CO_2 Field Lab on Svalbard, Arctic Norway. The Rurikfjellet Formation was deposited in an open marine environment with regressive succession under oxic conditions [36,37] and it contains more carbonate and less organic carbon than the Draupne core (Table 1). Distinctive features of sideritic nodules and thin shale beds are commonly cemented by siderite (Figure 5).
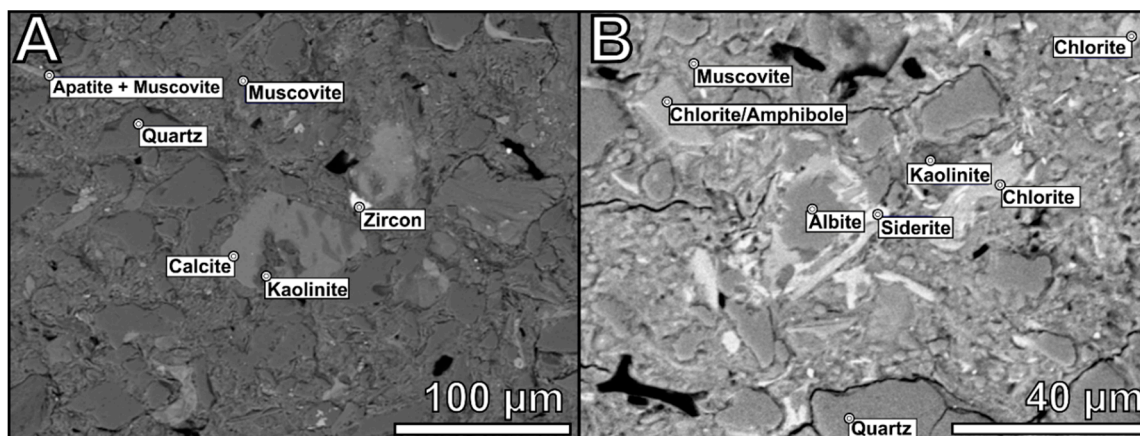

Figure 5. SEM imaging of Rurikfjellet Shale samples from 308 m depth (**A**) and another from 369 m depth (**B**) (modified after [38]).

The Rurikfjellet core was retrieved from 385 m depth in borehole Dh4 [38]. The core sample was encapsulated in aluminium and paraffin immediately after coring. One cylindrical core specimen, LYB22, with a diameter of 40 mm, nominal length 70 mm was prepared for testing within the direct shear box once removed from the encapsulating material. A fracture was manually induced in the

middle of the specimen parallel with the bedding plane using a sharp blade. The water content of the test specimen was about 3% prior to testing.

3.2. Test Procedure

A direct shear apparatus was used for testing the fractured shale samples. The vertical (normal) and horizontal (shear) forces were applied through two independent actuators. During shearing, the lower box moves whereas the upper box is kept stationary (Figure 4). The vertical load was measured with a load sensor installed inside the vertical load actuator just above the upper shear box, and vertical displacement was measured by four linear variable displacement transducers (LVDTs) recording the change in distance between the top and bottom box. The shear force was measured with a load sensor installed between the horizontal actuator and the lower box. Horizontal deformation was measured by four LVDTs attached to the top box, measuring the change in distance between the top and bottom box. The precision of both the vertical and horizontal deformation sensors was 0.0002 mm. More details of the set-up are available in [39].

The direct shear test (DST) was run according to the ASTM standard [40]. An intentional modification was made here regarding the shearing velocity, to investigate the velocity-dependent frictional properties. The shear velocity was changed during the shearing of each sample in what is known as velocity-stepping direct shear tests (as described in Section 4). Constant normal load (CNL) procedure was adopted for Draupne specimen DST15 and Rurikfjellet LYB22 while constant normal stress (CNS) procedure was applied to Draupne DST17. In the CNL procedure, the normal load was kept constant during the velocity stepping. The normal load was then increased, before the velocity-stepping procedure was repeated. A total of three different normal loads and three different velocity-stepping cycles (nine shear phases in total) were included for both samples DST15 and LYB22. We note that as the contact area decreases during shearing in the CNL procedure, the normal stress on the specimen will increase as shearing progresses under a constant normal load. Therefore, the actual contact area during shearing has been calculated for all tests, and all normal (and shear) stresses reported in this study are corrected for the change of contact areas. For the CNS test procedure (DST17), the normal stress was kept constant during the velocity-stepping phase of the test. The following steps summarize the test procedure followed for the experiments presented in this paper:

- *Mounting specimen in shear box*: The prepared bottom and top parts of the specimens were cast into the bottom and top boxes of the shear apparatus using a composite epoxy. The shear box was assembled to fit the two parts of the specimen together. The epoxy was allowed to cure for 24 h. During the curing period, the specimens were covered with a thin layer of plastic and oil to avoid drying. An unconfined gap of approximately 8 mm was allowed between the top and bottom boxes. The specimens were prepared and inserted into the shear box so that fracture plane was near-horizontal and located at the mid-height of the unconfined gap. This ensured that the fracture could slide freely along the horizontal plane during shearing (Figure 4).

- *Application of normal load and sample seating*: The normal load or stress applied to the specimens was estimated based on the representative normal stress acting on fractures at in situ conditions. A pre-loading phase was included in the shear tests to assure good seating of the two parts of the specimens. For this, the normal stress was increased to around 10% of the unconfined compressive strength of the intact material. The load was then decreased, before reloading to the target normal load.

- *Velocity-stepping and slide-hold-slide (SHS) shear tests*: General procedures for velocity-stepping and SHS tests are described in [5,6,12,41]. The specific procedure followed for Draupne and Rurikfjellet tests are described below:

  1. For both Draupne samples (DST15 and DST17), the test procedure was a combination of velocity-stepping and slide-hold-slide testing. Following application of a normal load (for DST15) and normal stress (for DST17), an initial shearing phase was conducted at a

low shear velocity. Next, shearing was stopped for a given time period before re-shearing at a different velocity. The hold-time periods between shearing phases were constant for each test; 2 min for DST15 and 5 min for DST17. This is different to the regular SHS test procedure [12], where the duration of hold-time is changed during the test.

2. For the Rurikfjellet specimen (LYB22), the shear velocity was changed whilst shearing the sample, i.e., no hold-time was included. Three shear velocities were used at three different constant normal loads.

3.3. Characterization of Fracture Surface

Topography of the fracture surfaces was characterised for Draupne samples using photogrammetry before and after testing to analyse the impact of shearing on surface morphology. Such an analysis could not be performed for the Rurikfjellet specimen because of the lack of appropriate images before testing. The principle of photogrammetry consists of two successive steps after acquiring the necessary images. The first step comprises of the detection and matching of automatic tie points [42]. A tie point is a point that has ground coordinates that are not known but is recognisable in at least two images because of the local features in the overlap area between the images. This means that pixels displaying strong local contrast (known as feature points) are detected and described, and feature points from different images with similar descriptors are automatically identified and therefore constitute tie points. The second step corresponds to a bundle adjustment [43], where the relative locations of viewpoints (camera positions) are computed. The result of this second step is then used to reconstruct the final model of the photographed object using image correlation. In this study we use the versatile, accurate, and free open-source software MicMac [42–44] to implement the photogrammetry algorithms. The results of the photogrammetry, and a comparison between the profiles of fracture surfaces before and after testing are provided in Section 4.1.

The roughness of a fracture plane may be described by the joint roughness coefficient (*JRC*) which is a parameter in the Barton–Bandis peak strength criterion [45]. From the photogrammetric data, the *JRC* was calculated using the roughness algorithm, *Z2* [46]:

$$Z2 \; = \; \left[\frac{1}{L} \int_{x=0}^{x=L} \left(\frac{dy}{dx} \right)^2 dx \right] \; = \; \left[\frac{1}{L} \sum_{i=1}^{n-1} \frac{(y_{i+1} - y_i)^2}{(x_{i+1} - x_i)} \right]^{1/2} \tag{5}$$

The roughness algorithm is further related to the *JRC* by the following relation [47]:

$$JRC \; = \; 51.85 \times Z2^{0.6} - 10.37 \tag{6}$$

where *Z2* is the root mean square of the first derivative of the profile, *L* is the length of the profile, x_i is an arbitrary point on x-coordinate and y_i is an arbitrary point on y-coordinate (asperity height).

4. Results

4.1. Impact of Shearing on Fracture Topography

Figure 6 presents the reconstructed topography for the lower part of Draupne specimen DST15 pre- and post-test. The surface topography pre-test could only be partially reconstructed because of insufficient overlapping between images in some locations (shown by the blue stripes in Figure 6-upper left). Two cross sections, plotted using the MicMac software, showing the topography are presented below the 2D map in Figure 6; sections A1 and A2 are pre-test and B1 and B2 are post-test. Both cross-sections are parallel to the right-to-left direction of shearing. Comparing the cross-sections before and after shearing, we observe slight changes in the fracture surface (roughness), indicating cutting off fracture asperities during the test (A1 compared with B1, for example), whereby the post-test fracture surface is slightly smoother than the pre-test fracture surface. The *JRC* values for

the two selected profiles were around 1 and 9 pre-test, whereas they were around 0.5 and 6 post-test, respectively (see Figure 6). The degradation in roughness may be described by the reduction in joint roughness coefficient [45], which in this case is further calculated from the roughness parameter Z2 [46] (Figure 6).
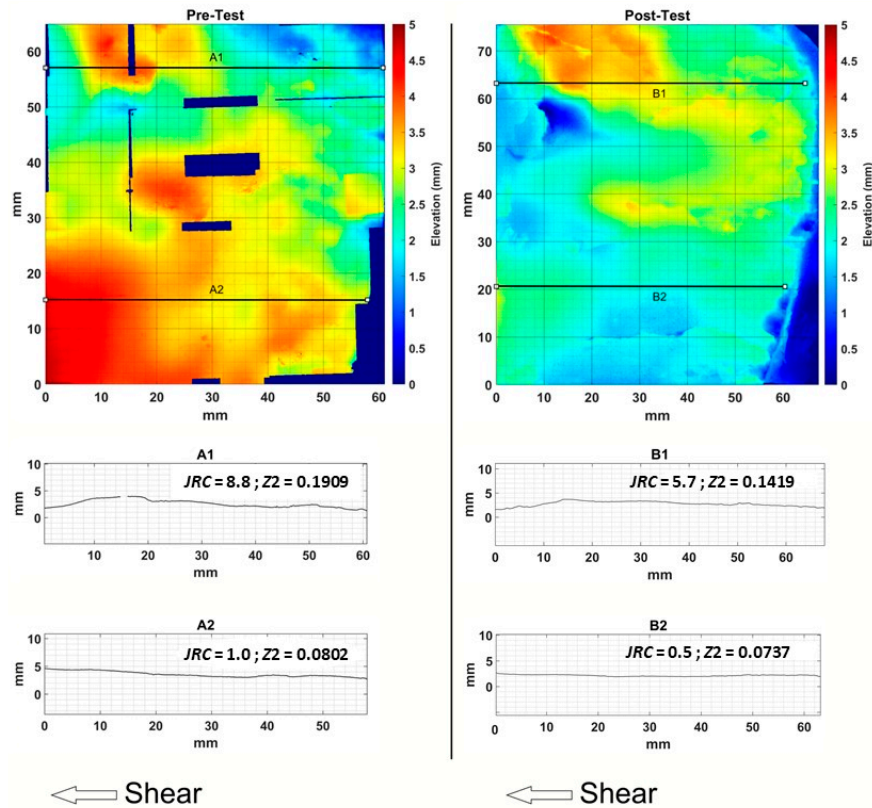

Figure 6. Topography of the fracture surface before and after the direct shear test (Draupne DST15). The arrow on the figure shows the direction of shearing. The roughness values of *JRC* and *Z*2 are portrayed with their respective profile.

Similarly, Figure 7 shows the pre- and post-test morphology of DST17's fracture surface. Cross sections A1 and A2 present surface profiles before testing in the shear box, while B1 and B2 show the topography of the same profiles after testing. The change in topography before and after testing is minor for both profiles. Because of the smooth nature of the fracture plane, the relationship used in this case for estimating *JRC* (Equation (6)) produces negative values for most of the profiles taken parallel to the shear direction. The negative values of *JRC* presented in these profiles (Figure 7) are equivalent to zero in the Barton–Bandis roughness chart. The *JRC* values of DST17 are shown together with their respective profiles in Figure 7. Comparison between the two Draupne specimens shows that the fracture topography of DST15 was more altered during shearing (Figure 6). This may be a consequence of the high normal stresses applied during testing of DST15 (18–35 MPa) compared with DST17 (1–18 Mpa). Application of higher normal stress may have resulted in greater crushing of the asperities for sample DST15.
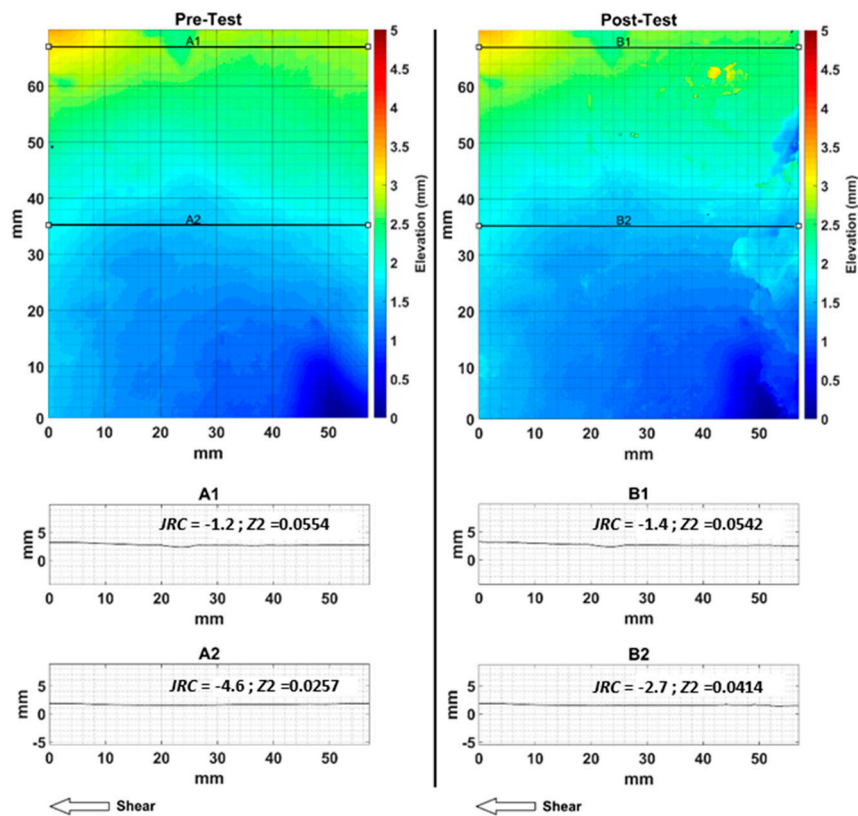
Figure 7. Topography of the fracture surface before and after the direct shear test (Draupne DST17). The arrow on the figure shows the direction of shearing. The roughness values of *JRC* and Z2 are portrayed with their respective profile. The negative values of *JRC* are equivalent to zero in the Barton-Bandis roughness chart.

4.2. Frictional Properties at Various Shear Velocities for Draupne

Results of the velocity-stepping direct shear tests on the two Draupne shale specimens are presented in Figure 8. Specimen DST15 was tested under constant normal load and thus the corrected normal stress increased proportional to shear displacement as shown in Figure 8a,b. Under each normal stress (marked stages A-C in the figure), the sample was sheared 2 mm at three different shear velocities (V_1 = 1, V_2 = 10 and V_3 = 50 μm/s). For all stages of shearing, a rapid initial increase in shear stress was observed before static friction was overcome, following which shear stress remained quasi-constant during steady-state sliding. For each normal stress we observed an increase in shear stress with increasing shear velocity (Figure 8a). Similar to the shear stress, the friction coefficient (calculated as the ratio of shear stress to normal stress) increased rapidly at the start of shearing, before levelling off (Figure 8b). When the shear velocity was increased from V_1 to V_2 the first time, the direct effect on the friction coefficient was an increase from around 0.22 to 0.26, before stabilizing at around 0.25. For the next velocity step, the friction coefficient increased from 0.25 to around 0.28 shortly after the application of shear velocity V_3. A similar trend of increasing friction coefficient was observed for stages B and C at higher normal stress levels and at higher cumulative shear displacements (Figure 8b). The observed increase in friction coefficient with increasing shear velocity for Draupne DST15 indicates velocity-strengthening behaviour.
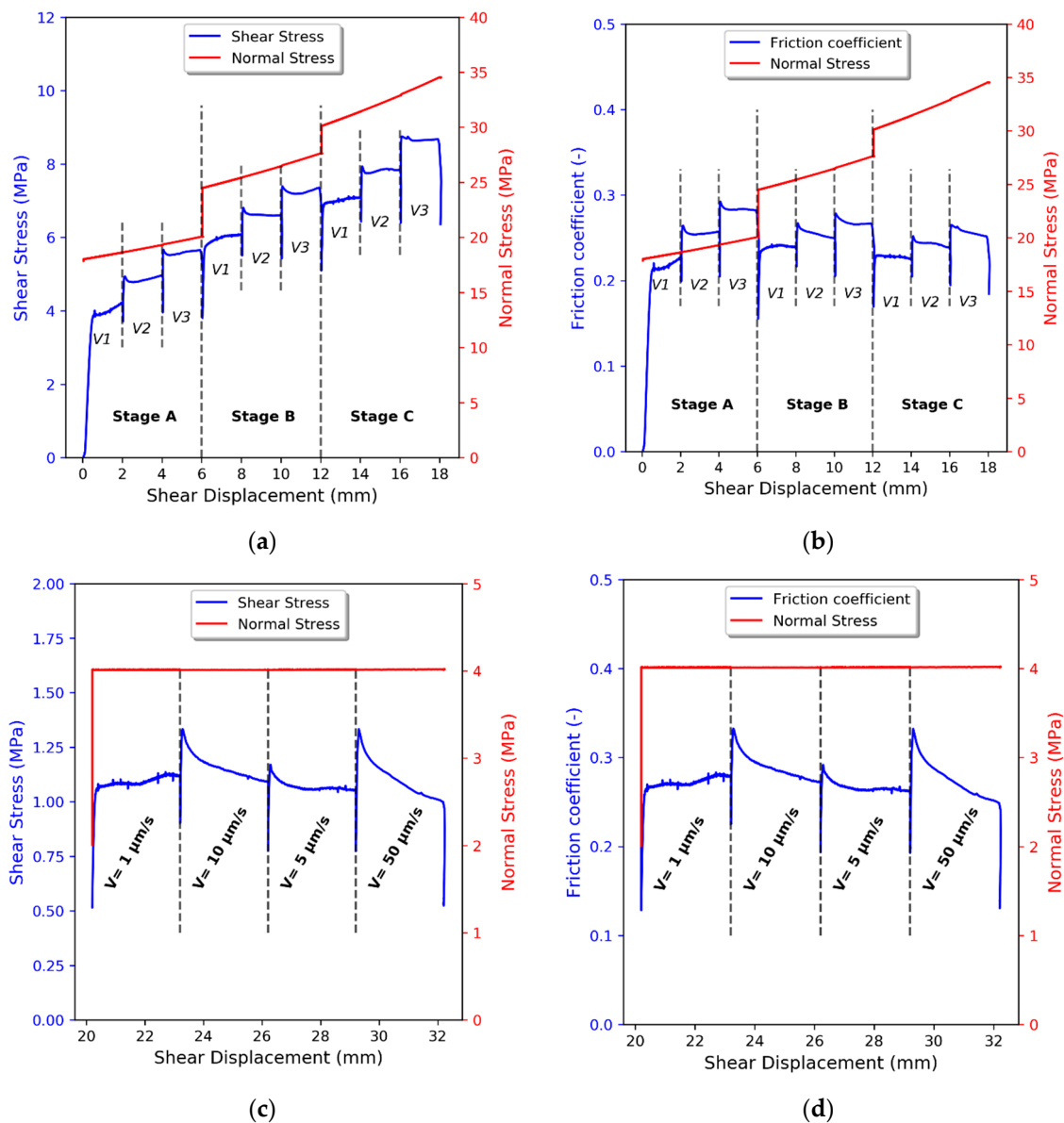
Figure 8. Evolution of shear stress and friction coefficient versus shear displacement for Draupne DST15 (**a**,**b**) following the constant normal load procedure at three different shear velocities ranging from 1 to 50 μm/s and (**c**,**d**) Draupne DST17 with constant normal stress procedure at four different shear velocities ranging from 1 to 50 μm/s.

The DST17 specimen was first sheared under different normal stresses at a constant shear velocity for the first 20 mm of horizontal displacement, before beginning the velocity-stepping procedure. Four different shear velocities were used under a constant normal stress of 4 MPa (Figure 8c,d). Each shear velocity step comprised of 3 mm of horizontal displacement. The velocity steps included an increase from 1 to 10 μm/s then a decrease to 5 μm/s followed by another increase to 50 μm/s. This procedure was adopted to investigate the response of the friction parameters to both increase and decrease of slip velocity. The shear stress showed an immediate increase to about 1.1 MPa (called direct-effect) before levelling off during the first shear velocity of 1 μm/s. The increase in shear velocity to 10 μm/s was accompanied by a direct-effect of around 0.2 MPa increase of shear stress. The third step involved a decrease in shear velocity and the resulting direct-effect was noticeably smaller on the shear stress than for the case of increasing shear velocity. Lastly, the shear velocity was increased again, and the direct-effect was again substantial; around 0.25 MPa.

The friction coefficient of specimen DST17 reached around 0.27 during the first velocity step and increased to around 0.28 over a shear displacement of 3 mm (Figure 8d). Development of the friction coefficient versus shear displacement shows a similar increase as that of the shear stress. The direct-effect of velocity change is observed as an increase in friction coefficient. The residual friction at the velocity of 10 µm/s is almost the same as that for the velocity of 1 µm/s. When shear velocity was reduced to half, friction coefficient showed a small direct-effect but decreased again and reached about the same value as for the previous step. When the shear velocity was increased from 5 to 50 µm/s, the direct effect was large but the residual friction dropped to about the same value as that for the velocity of 5 µm/s.

The variation in friction rate parameter $(a - b)$ for the Draupne specimens is presented in Figure 9. For DST15, $(a - b)$ is positive for all velocity steps and under all normal stresses applied in stages A–C (Figure 9a). Again, this is velocity-strengthening behaviour. This behaviour implies slip on a natural fracture, as in DST15, will be aseismic. For DST17, which contained an induced fracture, $(a - b)$ plots both above and below 0 (Figure 9b). Although the negative values are very close to zero, it may imply that the response of an induced, fresh fracture to velocity-stepping test (DST17) may be different from that of an existing fault plane (DST15).
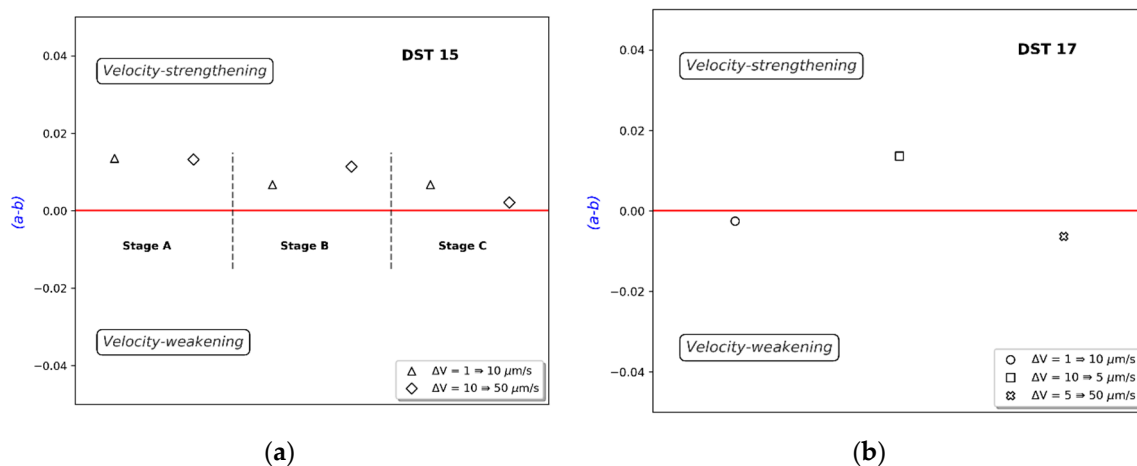

(a)　　　　　　　　　　　　　　　　　　　　　　　　　　(b)

Figure 9. Friction rate parameter $(a - b)$ for Draupne shale specimens showing the evolution of friction when a change of shear velocity is introduced. DST15 contains a pre-existing fault plane (**a**) and DST17 includes a laboratory-induced fracture (**b**). Negative values show velocity-weakening and thus imply potential for seismic slip, while positive values show velocity strengthening and potentially aseismic slip.

Another parameter of interest is the change of the friction coefficient during hold-times, i.e., immediately after stopping the shear phase in slide-hold-slide (SHS) tests (see Figure 2b). The reduction in friction once shearing is ceased, is represented by the frictional relaxation $(\Delta\mu_c)$, and has been shown to increase linearly with logarithmic hold time [12]. In DST15 (hold time = 2 min) and DST17 (hold time = 5 min) the hold times between subsequent shear phases were constant. Here, it was the shear velocity before holding, and the normal stress during holding which were varied in the experiments. Figure 10 shows the frictional relaxation for the Draupne specimens as a function of the applied normal stress (Figure 10a), and shear velocity (Figure 10b) prior to the hold periods. Overall, DST17 shows more stress relaxation, in agreement with what is expected for longer hold times (Figure 10). Furthermore, there is a tendency towards decreasing frictional relaxation $(\Delta\mu_c)$ as normal stress increases (Figure 10a). In contrary, the magnitude of frictional relaxation increases with increasing shear velocity before hold times for both samples (Figure 10b). This is consistent with other studies documented in for example [12]. Frictional relaxation during hold periods is mainly due to creep. At higher normal stress creep could be counteracted, and this may explain the decrease of $\Delta\mu_c$ with increasing normal stress.
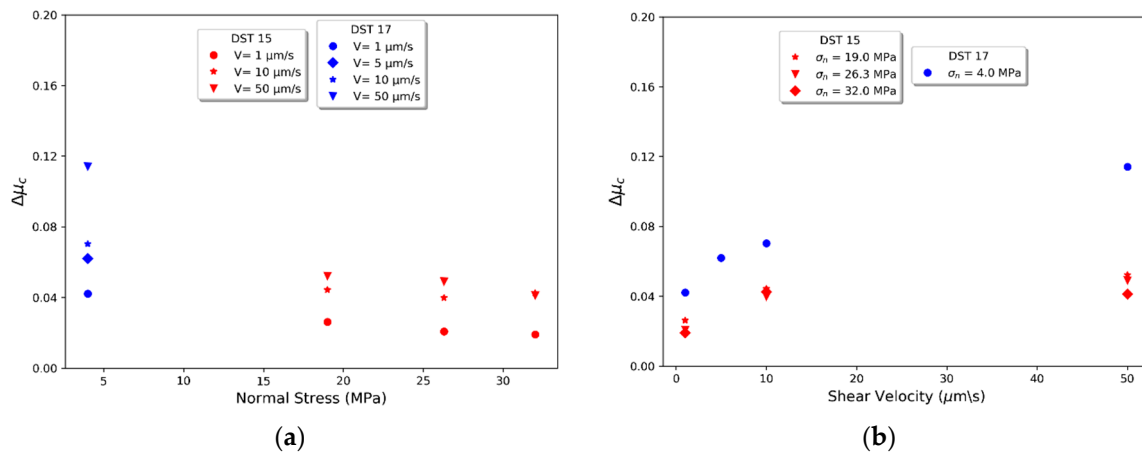
(**a**)   (**b**)

Figure 10. Frictional relaxation ($\Delta\mu_c$) against normal stress (**a**) and shear velocity (**b**) for Draupne specimens. Frictional relaxation decreases with increasing normal stress, but increases with increasing shear velocity before holding.

The post-peak frictional weakening ($\Delta\mu_w$) is the difference between peak friction after restarting shear and the friction once steady state sliding is achieved (see illustration in Figure 2b). Figure 11 shows the relationship between frictional weakening and normal stress for the Draupne specimens. As for frictional relaxation, the magnitude of frictional weakening is greater for DST17. Overall, $\Delta\mu_w$ decreases with increasing normal stress and shows a positive correlation to shear velocity at low normal stress (4 MPa); i.e., the higher the shear velocity, the higher the frictional weakening. The sensitivity to shear velocity also appears to diminish as normal stress increases.
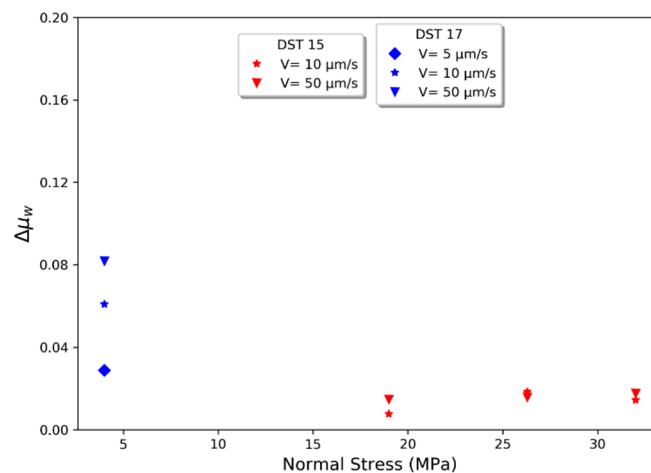
Figure 11. Relationship between frictional weakening and applied normal stress for the Draupne specimens. For low normal stress, the higher the shear velocity, the higher is the magnitude of frictional weakening. For higher normal stress, frictional weakening does not show any clear dependency on the shear velocity.

4.3. Frictional Properties at Various Shear Velocities for Rurikfjellet Shale

The Rurikfjellet specimen (LYB22) was sheared under three different constant normal loads (CNL), leading to the increased corrected normal stress seen in Figure 12. For every normal load stage (A to C in Figure 12), the sample was sheared with three different shear velocities ($V_1 = 1$, $V_2 = 10$ and $V_3 = 50$ μm/s). The first 1 mm of horizontal displacement was sheared at 1 μm/s, followed by 0.5 mm horizontal displacement at 10 and 50 μm/s. LYB22 was tested according to a more typical velocity-stepping procedure, with no hold time in shearing between the different velocity steps. However, shearing was stopped between stages when the normal load was increased. During stage A,

the shear stress changed only slightly when the shear velocity was increased from 1 to 10 μm/s and from 10 to 50 μm/s (Figure 12a). After increasing the normal load and entering stage B, a pronounced direct-effect was seen when shearing was restarted at the lowest shear velocity. A slight increase in the steady state shear stress and friction coefficient was observed for the steps with higher shear velocity. After shearing was stopped at the end of stage B and the normal load increased to the level specified at stage C, the direct effect upon restarting slow shearing in stage C was again clear. The further shear stress development during stage C was more complex. About halfway into the first shearing with the low velocity, a sharp decline in shear stress was measured which was likely due to the generation of a large fracture, which was discovered after testing. Increasing the shear velocity to 10 and 50 μm/s caused both minor direct and evolutionary effects leading to an increase in shear stress and friction coefficient.

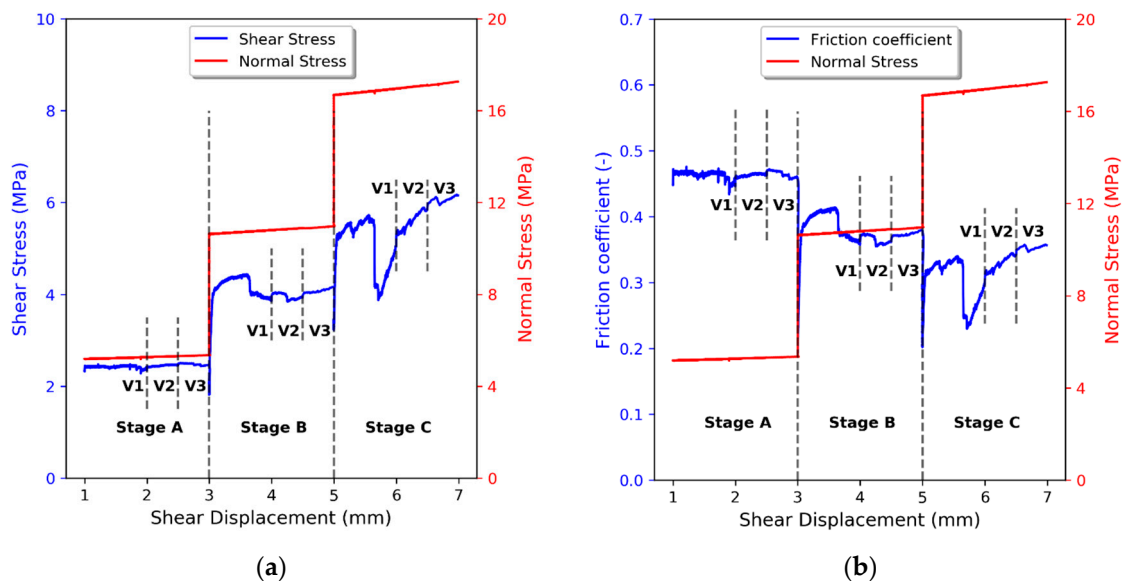(**a**)　　　　　　　　　　　　　　　　　　　　　(**b**)

Figure 12. Results of the velocity-stepping direct shear tests on a laboratory-induced, bedding-parallel fracture for Rurikfjellet shale specimen LYB22. Evolution of shear stress (**a**) and friction coefficient (**b**) versus shear displacement at different normal stresses and at various shear velocities.

The friction rate parameter (*a* − *b*) was calculated for all velocity steps of the Rurikfjellet specimen LYB22 (Figure 13). The calculation was done for three stages and for the velocity change from 1 to 10 μm/s and from 10 to 50 μm/s. For five out of the six velocity steps, positive (*a* − *b*) values pointed towards velocity-strengthening and the potential for aseismic behaviour during a slip.
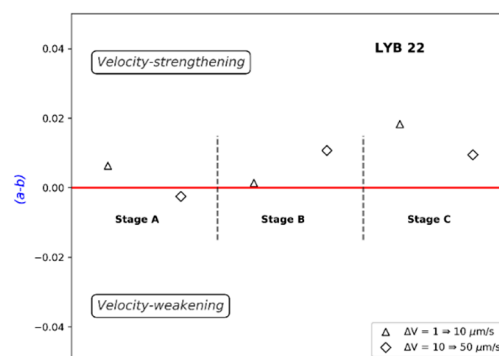

Figure 13. Friction rate parameter (*a* − *b*) for Rurikfjellet specimen (LYB22). Positive values show velocity-strengthening and thus imply aseismic slip and negative values show velocity-weakening and seismic slip.

5. Discussion

5.1. The Impact of Shear Velocity on Frictional Properties of Draupne and Rurikfjellet Shales

The present study shows how the change of shear velocity during a direct shear test affects the frictional parameters of Draupne and Rurikfjellet shale samples. For both shales, we observed an immediate increase (direct-effect) of friction coefficient upon increasing the shear velocity. This was also true when we re-sheared the samples at a velocity lower than the velocity of the preceding step (Figure 8c,d). In addition to the direct-effect, the change in shear velocity also affects friction in the residual phase (evolutionary effect) which follows the peak values. We show these changes in terms of $(a - b)$ parameter as described in Section 2. The friction rate parameter $(a - b)$ obtained for Draupne specimen DST15 was positive for all the steps of the test. This specimen contained a pre-existing fault plane. For the other Draupne specimen, DST17, the $(a - b)$ was positive for one step and negative (close to zero) for the other two. This specimen contained a laboratory-induced fresh fracture. This may indicate that slip on faults in the Draupne Formation might follow the velocity-strengthening concept. Fault rocks that show velocity-strengthening cannot generate accelerating slip, and are thus not capable of generating earthquakes [12,28,29]. Hence, these results may also imply that there will be a difference between pre-existing fault planes and newly created fractures in the Draupne Formation. For the Rurikfjellet specimen LYB22, which also contained a laboratory-induced fracture, the value of $(a - b)$ was positive for five out of the six steps tested (Figure 13). Again, this is an indication of velocity-strengthening. Thus we may conclude that a failure and slip on fractures in Rurikfjellet Formation may also be associated with slow, aseismic movement.

5.2. Impact of Mineralogy on Frictional Properties

Mineralogy may also be used to evaluate the seismic potential of rocks [20]. Ikari, et al. [48] examined the correlation between friction coefficient and the $(a - b)$ parameter for several types of rocks and minerals. They found that materials with a friction coefficint lower than 0.5 generally showed positive $(a - b)$ values, whereas materials with higher friction coefficients could display both positive and negative $(a - b)$ values (Figure 14a). The friction coefficient for Draupne specimens were roughly between 0.20 and 0.30 and for Rurikfjellet specimen around 0.25–0.45 throughout the tests. Thus, response of these rocks are in agreement with the data cloud of positive $(a - b)$ values postulated by Figure 14a. Figure 14b presents stable and unstable friction zones in a ternary plot based on three categories of minerals. The upper, blue section indicates a 'stable friction' zone where the content of clay and organic matter is higher than 40%. The zone in red in the same figure gives the mineralogical outline of materials that are more prone to seismic slip. Both the Draupne and Rurikfjellet shales have clay+organic content >40% (see Table 1) that place them in the blue, stable friction zone of the ternary diagram. This implies if a slip occurs on such a material the movement will most likely be aseismic. This is another indication which is consistent with the velocity-strengthening behaviour of the Draupne and Rurikfjellet shales reported in this paper.
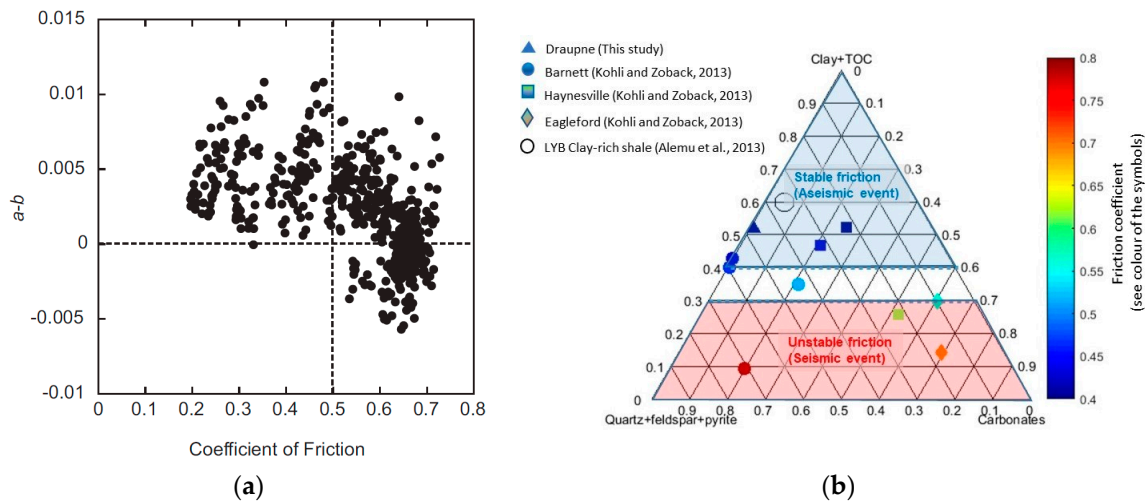
Figure 14. (**a**) correlation between the friction rate parameter ($a - b$) and the coefficient of friction (after [48]). The data in the plot (**a**) represent a wide range of materials. (**b**) Ternary plot of mineralogy and its relation to seismic potential of rocks (modified after [20]) with the Draupne and Rurikfjellet shales included. The colour bar shows the friction coefficient.

5.3. Implications from Acoustic Emission Study on Draupne Shale

Another laboratory study on the Draupne shale samples was performed by Griffiths et al. [49] where they monitored acoustic emission (AE; laboratory-scale seismicity) events during the triaxial testing of rock cores. AE monitoring was performed during both isotropic and anisotropic loading, undrained shearing to failure and subsequent reactivation of the shear fracture created during the triaxial test. The observation was that no AE was generated from any of the phases mentioned above. AE events measured in laboratory are proxies to seismic events in field conditions. The absence of AE events in the laboratory experiments described implies that the potential of seismicity for the Draupne shale during slip is very low. This also agrees well with the results presented in this paper.

It should be noted that the fractures subjected to the velocity-stepping direct shear tests in this study were clean without any gouge material on them at the beginning of the test. In real in situ conditions, fractures are usually filled with fine particles (gouge material) [50] which could potentially change the material friction [24]. Therefore, before extrapolating these experimental results to field conditions, the frictional properties of infilled Draupne and Rurikfjellet fractures should be investigated.

6. Conclusions

Core samples of the Draupne and Rurikfjellet cap rock shales were subjected to velocity-stepping and slide-hold-slide tests to investigate their velocity-dependence frictional properties. Under a range of normal stresses representing in situ stresses acting on fractures and faults in the field, samples were sheared in a direct shear apparatus at shear velocities ranging from 1 to 50 μm/s. It was found that the frictional relaxation correlates with both the applied normal stress and shear velocity for the Draupne shale. The higher the applied normal stress, the lower the magnitude of frictional relaxation. Frictional relaxation was positively correlated with shear velocity applied before hold-time phases: the higher the shear velocity, the greater the magnitude of frictional relaxation. Furthermore, it was observed that frictional weakening increases with increasing shear velocity but is negatively correlated with normal stress. The correlations were observed in both Draupne tests, i.e., for both pre-existing fault and laboratory-induced fractures. The friction rate parameter ($a - b$) was calculated and used to evaluate the response of material friction to velocity change. The magnitude of ($a - b$) increased for both shales with increasing shear velocity, indicating a velocity-strengthening behaviour for most of the cases tested. Velocity-strengthening implies that accelerating slip, that generate seismicity, cannot occur during failure and slip. The results of this study imply that a failure and slip of (clean) fractures in the

Draupne and Rurikfjellet formations will most likely not generate seismic events. Other indicators such as mineralogical composition and acoustic emission tests performed on Draupne shale by other researchers also confirm the likelihood of aseismic slip for both Draupne and Rurikfjellet formations. Thus, possible failure of these formations may not be detected by methods relying on monitoring seismic slip only. To ensure integrity of CO_2 storage reservoirs, a combination of monitoring methods, that can also detect aseismic movement of fractures and faults, is recommended.

References

1. Rogelj, J.; Shindell, D.; Jiang, K.; Fifita, S.; Forster, P.; Ginzburg, V.; Handa, C.; Kheshgi, H.; Kobayashi, S.; Kriegler, E. Chapert 2: Mitigation pathways compatible with 1.5 c in the context of sustainable development. In *Global Warming of 1.5 °C an Ipcc Special Report on the Impacts of Global Warming of 1.5 °C above Pre-Industrial Levels and Related Global Greenhouse Gas Emission Pathways, in the Context of Strengthening the Global Response to the Threat of Climate Change*; Intergovernmental Panel on Climate Change: Geneva, Switzerland, 2018.

2. Majer, E.L.; Baria, R.; Stark, M.; Oates, S.; Bommer, J.; Smith, B.; Asanuma, H. Induced seismicity associated with enhanced geothermal systems. *Geothermics* **2007**, *36*, 185–222. [CrossRef]

3. Segall, P. Earthquakes triggered by fluid extraction. *Geology* **1989**, *17*, 942–946. [CrossRef]

4. Nicol, A.; Walsh, J.; Villamor, P.; Seebeck, H.; Berryman, K. Normal fault interactions, paleoearthquakes and growth in an active rift. *J. Struct. Geol.* **2010**, *32*, 1101–1113. [CrossRef]

5. Simpson, D.; Leith, W.; Scholz, C. Two types of reservoir-induced seismicity. *Bull. Seismol. Soc. Am.* **1988**, *78*, 2025–2040.

6. Van Eijs, R.; Mulders, F.; Nepveu, M.; Kenter, C.; Scheffers, B. Correlation between hydrocarbon reservoir properties and induced seismicity in the netherlands. *Eng. Geol.* **2006**, *84*, 99–111. [CrossRef]

7. Hubbert, K.K.; Rubey, W.W. Role of fluid overpressure in mechanics of overthrust faulting. *Geol. Soc. Am. Bull.* **1970**, *70*, 583–586.

8. Pluymakers, A.M.; Samuelson, J.E.; Niemeijer, A.R.; Spiers, C.J. Effects of temperature and CO_2 on the frictional behavior of simulated anhydrite fault rock. *J. Geophys. Res. Solid Earth* **2014**, *119*, 8728–8747. [CrossRef]

9. Samuelson, J.; Spiers, C.J. Fault friction and slip stability not affected by CO_2 storage: Evidence from short-term laboratory experiments on north sea reservoir sandstones and caprocks. *Int. J. Greenh. Gas Control* **2012**, *11*, S78–S90. [CrossRef]

10. Ikari, M.J.; Carpenter, B.M.; Marone, C. A microphysical interpretation of rate-and state-dependent friction for fault gouge. *Geochem. Geophys. Geosyst.* **2016**, *17*, 1660–1677. [CrossRef]

11. Hunfeld, L.; Niemeijer, A.; Spiers, C. Frictional properties of simulated fault gouges from the seismogenic groningen gas field under in situ p–t-chemical conditions. *J. Geophys. Res. Solid Earth* **2017**, *122*, 8969–8989. [CrossRef]

12. Chen, J.; Verberne, B.A.; Spiers, C.J. Effects of healing on the seismogenic potential of carbonate fault rocks: Experiments on samples from the longmenshan fault, sichuan, china. *J. Geophys. Res. Solid Earth* **2015**, *120*, 5479–5506. [CrossRef]

13. Carpenter, B.; Marone, C.; Saffer, D. Weakness of the San Andreas fault revealed by samples from the active fault zone. *Nat. Geosci.* **2011**, *4*, 251–254. [CrossRef]

14. Carpenter, B.M.; Ikari, M.J.; Marone, C. Laboratory observations of time-dependent frictional strengthening and stress relaxation in natural and synthetic fault gouges. *J. Geophys. Res. Solid Earth* **2016**, *121*, 1183–1201. [CrossRef]

15. Collettini, C.; Niemeijer, A.R.; Viti, C.; Smith, S.A.; Marone, C. Fault structure, frictional properties and mixed-mode fault slip behavior. *Earth Planet. Sci. Lett.* **2011**, *311*, 316–327. [CrossRef]

16. Niemeijer, A.R.; Collettini, C. Frictional properties of a low-angle normal fault under in situ conditions: Thermally-activated velocity weakening. *Pure Appl. Geophys.* **2014**, *171*, 2641–2664. [CrossRef]

17. Dieterich, J.H. Modeling of rock friction: 1. Experimental results and constitutive equations. *J. Geophys. Res. Solid Earth* **1979**, *84*, 2161–2168. [CrossRef]

18. Ruina, A. Slip instability and state variable friction laws. *J. Geophys. Res. Solid Earth* **1983**, *88*, 10359–10370. [CrossRef]

19. Marone, C. Laboratory-derived friction laws and their application to seismic faulting. *Annu. Rev. Earth Planet. Sci.* **1998**, *26*, 643–696. [CrossRef]

20. Kohli, A.H.; Zoback, M.D. Frictional properties of shale reservoir rocks. *J. Geophys. Res. Solid Earth* **2013**, *118*, 5109–5125. [CrossRef]

21. Marone, C.; Vidale, J.E.; Ellsworth, W.L. Fault healing inferred from time dependent variations in source properties of repeating earthquakes. *Geophys. Res. Lett.* **1995**, *22*, 3095–3098. [CrossRef]

22. Scholz, C.H. Earthquakes and friction laws. *Nature* **1998**, *391*, 37–42. [CrossRef]

23. He, C.; Wang, Z.; Yao, W. Frictional sliding of gabbro gouge under hydrothermal conditions. *Tectonophysics* **2007**, *445*, 353–362. [CrossRef]

24. Zoback, M.; Kohli, A.; Das, I.; Mcclure, M. The Importance of Slow Slip on Faults during Hydraulic Fracturing Stimulation of Shale Gas Reservoirs. In Proceedings of the SPE Americas Unconventional Resources Conference, Pittsburgh, PA, USA, 5–7 June 2012.

25. Das, I.; Zoback, M.D. Long-period, long-duration seismic events during hydraulic stimulation of shale and tight-gas reservoirs—Part 1: Waveform characteristicslpld events: Waveform characteristics. *Geophysics* **2013**, *78*, KS107–KS118. [CrossRef]

26. Warpinski, N.R.; Du, J.; Zimmer, U. Measurements of hydraulic-fracture-induced seismicity in gas shales. *Spe Prod. Oper.* **2012**, *27*, 240–252.

27. Dieterich, J.H. Time-dependent friction and the mechanics of stick-slip. *Pure Appl. Geophys.* **1978**, *116*, 790–806. [CrossRef]

28. Pluymakers, A.M. Frictional and Sealing Behavior of Simulated Anhydrite Fault Gouge Effects of CO_2 and Implications for Fault Stability and Caprock Integrity. Utrecht Series of Earth Sciences. Ph.D. Thesis, Utrecht University, Utrecht, The Netherlands, 2015.

29. Marone, C. The effect of loading rate on static friction and the rate of fault healing during the earthquake cycle. *Nature* **1998**, *391*, 69–72. [CrossRef]

30. Tadokoro, K.; Ando, M. Evidence for rapid fault healing derived from temporal changes in s wave splitting. *Geophys. Res. Lett.* **2002**, *29*, 6-1–6-4. [CrossRef]

31. Faleide, J.I.; Bjørlykke, K.; Gabrielsen, R.H. Geology of the norwegian continental shelf. In *Petroleum Geoscience*; Springer: Berlin/Heidelberg, Germany, 2010; pp. 467–499.

32. Mulrooney, M.J.; Osmond, J.L.; Skurtveit, E.; Faleide, J.I.; Braathen, A. Structural analysis of the smeaheia fault block, a potential CO_2 storage site, northern horda platform, north sea. *Mar. Pet. Geol.* **2020**, *121*, 104598. [CrossRef]

33. Skurtveit, E.; Grande, L.; Ogebule, O.; Gabrielsen, R.; Faleide, J.; Mondol, N.; Maurer, R.; Horsrud, P. Mechanical testing and sealing capacity of the upper jurassic draupne formation, north sea. In Proceedings of the 49th US Rock Mechanics/Geomechanics Symposium, San Francisco, CA, USA, 28 June–1 July 2015; American Rock Mechanics Association: Alexandria, VA, USA, 2015.

34. Zadeh, M.K. Compaction and Rock Properties of Siliciclastic Sediments-Implications for Reservoir Characterization, Velocity Anisotropy and Buildup of Abnormal Pore Pressure. Ph.D. Thesis, University of Oslo, Oslo, Norway, 2016.

35. Smith, H. Engineering Parameters of Draupne Shale-Characterization of Fractured Samples and Integration with Mechanical Tests. M.Sc. Thesis, University of Oslo, Oslo, Norway, 2019.

36. Braathen, A.; Balum, K.; Christiansen, H.; Dahl, T.; Eiken, O.; Elvebakk, H.; Hansen, F.; Hanssen, T.; Jochmann, M.; Johansen, T. The longyearbyen CO_2 lab of svalbard, norway-initial assessment of the geological conditions for CO_2 sequestration. *Nor. J. Geol.* **2012**, *92*, 353–376.

37. Olaussen, S.; Senger, K.; Braathen, A.; Grundvåg, S.-A.; Mørk, A. You learn as long as you drill; research synthesis from the longyearbyen CO_2 laboratory, svalbard, norway. *Nor. J. Geol.* **2019**, *99*, 157–181. [CrossRef]

38. Abbas, M. Geomechanical Characterization of Shale Caprock of the Longyearbyen CO_2 Storage Pilot. M.Sc. Thesis, University of Oslo, Oslo, Norway, 2015.

39. Bohloli, B.; Skurtveit, E.; Choi, J.C.; Grande, L.; Sauvin, G.; Soldal, M.; Wilkinson, H. Determination of shear properties and evaluation of fracture reactivation for a clay-rich shale: A case study from svalbard, arctic norway. *Bull. Eng. Geol. Environ.* **2020**, *79*, 4859–4872. [CrossRef]

40. ASTM. *Astm d5607-16 Standard Test Method for Performing Laboratory Direct Shear Strength Tests of Rock Specimens under Constant Normal Force*; ASTM International: West Conshohocken, PA, USA, 2016.

41. Niemeijer, A.; Spiers, C. Velocity dependence of strength and healing behaviour in simulated phyllosilicate-bearing fault gouge. *Tectonophysics* **2006**, *427*, 231–253. [CrossRef]

42. Lowe, D.G. Distinctive image features from scale-invariant keypoints. *Int. J. Comput. Vis.* **2004**, *60*, 91–110. [CrossRef]

43. Bretar, F.; Arab-Sedze, M.; Champion, J.; Pierrot-Deseilligny, M.; Heggy, E.; Jacquemoud, S. An advanced photogrammetric method to measure surface roughness: Application to volcanic terrains in the piton de la fournaise, reunion island. *Remote Sens. Environ.* **2013**, *135*, 1–11. [CrossRef]

44. Rupnik, E.; Daakir, M.; Deseilligny, M.P. Micmac—A free, open-source solution for photogrammetry. *Open Geospat. DataSoftw. Stand.* **2017**, *2*, 1–9. [CrossRef]

45. Barton, N.; Choubey, V. The shear strength of rock joints in theory and practice. *Rock Mech.* **1977**, *10*, 1–54. [CrossRef]

46. Tse, R.; Cruden, D.M. Estimating joint roughness coefficients. *Int. J. Rock Mech. Min. Sci. Geomech. Abstr.* **1979**, *16*, 303–307. [CrossRef]

47. Tatone, B.S.; Grasselli, G. A new 2d discontinuity roughness parameter and its correlation with jrc. *Int. J. Rock Mech. Min. Sci.* **2010**, *47*, 1391–1400. [CrossRef]

48. Ikari, M.J.; Marone, C.; Saffer, D.M. On the relation between fault strength and frictional stability. *Geology* **2011**, *39*, 83–86. [CrossRef]

49. Griffiths, L.; Dautriat, J.; Rodriguez, I.A.V.; Iranpour, K.; Sauvin, G.; Park, J.; Sarout, J.; Soldal, M.; Grande, L.; Oye, V. Inferring microseismic source mechanisms and in situ stresses during triaxial deformation of a north-sea-analogue sandstone. *Adv. Geosci.* **2019**, *49*, 85–93. [CrossRef]

50. Ogata, K.; Senger, K.; Braathen, A.; Tveranger, J.; Olaussen, S. Fracture systems and mesoscale structural patterns in the siliciclastic mesozoic reservoir-caprock succession of the longyearbyen CO_2 lab project: Implications for geological CO_2 sequestration in central spitsbergen, svalbard. *Nor. J. Geol. Nor. Geol. Foren.* **2014**, *94*, 121–154.